

1

# Physics-dynamics coupling with element-based high-order Galerkin 2 methods: quasi equal-area physics grid

3 Adam R. Herrington\*

4 *School of Marine and Atmospheric Sciences, Stony Brook University, Stony Brook, New York,  
5 USA.*

6 Peter H. Lauritzen

7 *Climate and Global Dynamics, National Center for Atmospheric Research, 1850 Table Mesa  
8 Drive, Boulder, Colorado, USA.*

9 Mark A. Taylor

10 *Sandia National Laboratories, Albuquerque, New Mexico, USA.*

11 Steve Goldhaber, Brian E. Eaton and Julio T. Bacmeister

12 *Climate and Global Dynamics, National Center for Atmospheric Research, 1850 Table Mesa  
13 Drive, Boulder, Colorado, USA.*

14 Kevin A. Reed

15 *School of Marine and Atmospheric Sciences, Stony Brook University, State University of New  
16 York, Stony Brook, New York.*

17 Paul A. Ullrich

<sup>18</sup> Department of Land, Air and Water Resources, University of California, Davis, California, USA.

<sup>19</sup> \*Corresponding author address: Adam R. Herrington, School of Marine and Atmospheric Sciences, Stony Brook University, Stony Brook, New York, USA.

<sup>20</sup> E-mail: adam.herrington@stonybrook.edu

## ABSTRACT

Atmospheric modeling with element-based high-order Galerkin methods presents a unique challenge to the conventional physics-dynamics coupling paradigm, due to the highly irregular distribution of nodes within an element and the distinct numerical characteristics of the Galerkin method. The conventional coupling procedure is to evaluate the physical parameterizations (*physics*) on the dynamical core grid. Evaluating the physics at the nodal points exacerbates numerical noise from the Galerkin method, enabling and amplifying local extrema at element boundaries. Grid imprinting may be substantially reduced through the introduction of an entirely separate, approximately isotropic finite-volume grid for evaluating the physics forcing. Integration of the spectral basis over the control-volumes provides an area average state to the physics, which is more representative of the state in the vicinity of the nodal points rather than the nodal point itself, and is more consistent with the notion of a ‘large-scale state’ required by conventional physics packages.

This study documents the implementation of a quasi-equal area physics grid into NCAR’s Community Atmosphere Model with Spectral Elements, and is shown to be effective at mitigating grid imprinting in the solution. The physics grid is also appropriate for coupling to other components within the Community Earth System Model, since the coupler requires component fluxes to be defined on a finite-volume grid, and one can be certain that the fluxes on the physics grid are indeed, volume-averaged.

43 **1. Introduction**

44 An increasing number of numerical methods publications in the atmospheric science literature  
45 concern transport, shallow-water, and three-dimensional models employing element-based high-  
46 order Galerkin discretizations such as finite-element and discontinuous Galerkin methods (for an  
47 introduction to these methods see, e.g., Durran 2010; Nair et al. 2011; Ullrich 2014). Some global  
48 models based on Galerkin methods have reached a level of maturity for which they are being con-  
49 sidered for next generation climate and weather models due to their inherent conservation proper-  
50 ties, high-order accuracy (for smooth problems), high parallel efficiency, high processor efficiency,  
51 and geometric flexibility facilitating mesh-refinement applications. NCAR’s Community Atmo-  
52 sphere Model (CAM; Neale et al. 2012) offers a dynamical core based on continuous Galerkin  
53 finite elements (Taylor and Fournier 2010), referred to as CAM-SE (CAM Spectral Elements;  
54 Taylor et al. 2008; Dennis et al. 2012; Lauritzen et al. 2018). CAM-SE is, in particular, being  
55 used for high resolution climate modeling (e.g., Small et al. 2014; Reed et al. 2015; Bacmeister  
56 et al. 2018) and static mesh-refinement applications (e.g., Fournier et al. 2004; Zarzycki et al.  
57 2014a,b; Guba et al. 2014b; Rhoades et al. 2016). Other examples of models based on high-order  
58 Galerkin methods that are being considered for ‘operational’ weather-climate applications are Gi-  
59 raldo and Restelli (2008), Nair et al. (2009), Brdar et al. (2013) and the Energy Exascale Earth  
60 System Model (<https://e3sm.org/>).

61 Assumptions inherent to the physical parameterizations (also referred to as *physics*) require  
62 the state passed by the dynamical core represent a ‘large-scale state’, for example, in quasi-  
63 equilibrium-type convection schemes (Arakawa and Schubert 1974; Plant and Craig 2008). In  
64 finite-volume methods (e.g., Lin 2004), one may think of the dynamical core state as the average  
65 state of the atmosphere over a control volume, and for resolutions typical of climate simulations

is entirely consistent with the notion of a ‘large-scale state’. For finite-difference methods (e.g., Suarez et al. 1983) the point value is thought of as representative for the atmospheric state in the vicinity of the point value and one can usually associate a volume with the grid-point. Hence the physics grid (the grid on which the state of the atmosphere is evaluated and passed to physics) and the dynamics grid (the grid the dynamical core uses) coincide. Having the physics and dynamics grids coincide is obviously convenient since no interpolation is needed (which could disrupt conservation properties) and the number of degrees of freedom on both grids is exactly the same.

For the regular latitude-longitude, cubed-sphere and icosahedral grids the distance between the grid-points is gradually varying for finite-volume/finite-difference discretizations. Examples of models that use these grids are CAM-FV (latitude-longitude grid, Lin 2004), FV3 (cubed-sphere grid, Putman and Lin 2007) and ICON (icosahedral grid, Wan et al. 2013). For high-order element-based Galerkin methods, the dynamical core grid is defined by the quadrature points. In CAM-SE, these are the Gauss-Lobatto-Legendre (GLL) quadrature nodes. A unique aspect of the high-order quadrature rules is that the nodes within an element are located at the roots of the basis set, which may be irregularly spaced. For example, Figure 1 shows GLL points on an individual element of a cubed-sphere grid for degree 3 ( $np \times np = 4 \times 4$  quadrature points) and degree 7 ( $np \times np = 8 \times 8$  quadrature points) Lagrange polynomial basis used in CAM-SE. The higher the order of the quadrature rule, the greater variance in distance between GLL quadrature points within an element. GLL quadrature points cluster near the edges and, in particular, the corners of the elements.

The resolved scales of motion are not determined by the distance between quadrature nodes, but rather the degree of the polynomial basis in each element. The nodes may be viewed as irregularly spaced samples of an underlying spectrally truncated state. From this perspective, one might expect the nodal solutions to be independent of location within an element. While the

90 interior quadrature nodes are  $C^\infty$  in CAM-SE (i.e. the basis representation is infinitely smooth  
91 and all derivatives are continuous), the smoothness of boundary nodes are constrained by the  
92 need to patch neighboring solutions together to form the global basis set, an operation known as  
93 the direct stiffness summation (DSS; Maday and Patera 1987; Canuto et al. 2007). The DSS  
94 operation is attractive because it allows for high-order accuracy with minimal communication  
95 between elements, but degrades the solution to  $C^0$  at element boundaries (i.e., all derivatives are  
96 discontinuous). Through evaluating the physics at the nodal points, strong grid-scale forcing or  
97 oscillatory behavior near an element boundary may exacerbate the discontinuity, and our initial  
98 expectation, that the nodal solutions are independent of within-element location, is unlikely for  
99 non-smooth problems, e.g., the presence of rough topography or moist physics grid-scale forcing.

100 It is the purpose of this paper to document the implementation of an entirely separate, quasi-  
101 equal area finite-volume physics grid into CAM-SE. The use of a separate physics grid is not  
102 entirely unheard of; prior studies have utilized the infrastructure developed for global-spectral  
103 transform methods to experiment with different physics grids (Williamson 1999; Wedi 2014). In  
104 our framework, the dynamical core state is integrated over control volumes to provide a volume av-  
105 eraged state to the physics, thereby minimizing the influence of any one particular nodal value on  
106 the physics forcing. Section 2 provides a thorough explanation of how grid imprinting manifests  
107 in high-order Galerkin methods for non-smooth problems. The implementation of the physics grid  
108 configuration into CAM-SE is presented in Section 3. Results from a hierarchy of idealized model  
109 configurations are presented in Section 4, illustrating the physics grid is effective at mitigating un-  
110 desirable grid imprinting in the solution. Section 5 contains a discussion of results and concluding  
111 remarks.

112 **2. The Quadrature Node Problem**

113 Figure 2 is a schematic illustrating in one-dimension how grid-imprinting is enabled by the  
114 physics, when the dynamical core is built using high-order Galerkin methods. The schematic  
115 depicts a time-step, starting from smooth initial conditions (Figure 2a), and subsequently advanc-  
116 ing the dynamics one Runge-Kutta time-step (Figure 2b). Since the boundary nodes of adjacent  
117 elements overlap one-another, there are now two solutions for each boundary node. The DSS op-  
118 erator, effectively a numerical flux applied to the element boundaries such that overlapping nodal  
119 values agree, is applied (Figure 2c), rendering the solutions at element boundaries  $C^0$ ; less-smooth  
120 than neighboring  $C^\infty$  interior nodes. An element boundary discontinuity may be exacerbated if,  
121 e.g., the physics updates the state at an element boundary (Figure 2d,e), resulting in characteristi-  
122 cally tighter gradients on the boundary nodes compared to if the physics forcing were applied to  
123 an interior node (Figure 2g,h).

124 To test the degree to which nodal solutions depend on within-element position, an aqua-planet  
125 simulation (Neale and Hoskins 2000; Medeiros et al. 2016), which consists of an ocean covered  
126 planet in perpetual equinox, with fixed, zonally symmetric sea surface temperatures idealized after  
127 the present day climatology, is carried out using CAM-SE, using CAM, version 4 physics (CAM4;  
128 Neale et al. 2010) and run for one year. The nominal low resolution *ne30np4* grid is used, pertain-  
129 ing to an average equatorial grid spacing of 111.2km. The probability density distribution of the  
130 upward vertical pressure velocity ( $\omega$ ), conditionally sampled based on three categories - ‘interior’,  
131 ‘edge’ and ‘corner’ nodes - is provided in Figure 3a. The motivation for assessing noise in the  $\omega$   
132 field comes from its connection with the atmosphere’s divergent modes, as follows from the con-  
133 tinuity equation in pressure coordinates. These modes are in turn sensitive to the within-element  
134 inhomogeneity of the pressure gradient that emerges from high-order Galerkin methods. There is

135 an apparent dependence on nodal location, with interior nodes being characteristically sluggish,  
136 and corner and edge nodes having systematically larger magnitude vertical motion. This behavior  
137 is consistent with the smoothness properties of the different nodal locations, with discontinuous  
138 pressure gradients resulting in greater vertical motion at edge and corner nodes. The main division  
139 of solutions shown in Figure 3a is primarily between whether a node is, or is not situated on an  
140 element boundary, and is a nuanced signature of high-order element-based Galerkin methods for  
141 non-smooth problems.

142 If the conventional physics-dynamics coupling paradigm is applied to CAM-SE, then the physics  
143 are to be evaluated at the GLL nodes, and a volume associated with the quadrature point should  
144 be defined. One approach to construct this grid is to decompose each spectral element into  
145  $(np - 1) \times (np - 1)$  subcells and then take the dual grid of this subcell grid. For cubed-sphere  
146 meshes, this dual grid will have a control volume associated with each quadrature point. These  
147 control volumes will be triangles for the cube corner quadrature points and quadrilaterals for all  
148 remaining quadrature points. Newton iteration can than be used to adjust the corners of these  
149 control volumes so that their spherical area exactly match the Gaussian weight multiplied by the  
150 metric term (these weights are used for integrating the basis functions over the elements and can  
151 therefore, in this context, be interpreted as areas). For cubed-sphere meshes, the Newton itera-  
152 tion can be replaced by a direct method if some of the quadrilaterals are replaced by pentagons  
153 giving additional flexibility in matching the spherical area to the quadrature weights. Such a dual  
154 grid is shown in Figure 4. This grid is used in the NCAR CESM (Community Earth System  
155 Model) coupler for passing states between ocean, atmosphere and land components since the cur-  
156 rent remapping method is finite-volume based and therefore requires control volumes (it is noted  
157 that methods exist that do not require control volumes for conservative interpolation, e.g., Ullrich  
158 and Taylor (2015)). Hence the components ‘see’ an irregular atmospheric grid. Similarly, the pa-

159 parameterizations in the atmosphere ‘see’ a state that is anisotropically sampled in space (see Figure  
160 1 and 5 in Kim et al. 2008).

161 The quadrature grid in element-based Galerkin methods is defined to perform mathematical  
162 operations on the basis functions, e.g., computing gradients and integrals, rather than evaluating  
163 the state variables for physics-dynamics coupling. One may argue that it would be more consistent  
164 to integrate the basis functions over quasi-equal area control volumes within each element and  
165 pass those control volume average values to physics rather than irregularly spaced quadrature point  
166 values. In this case when integrating basis functions over control volumes a grid-cell average value  
167 is more representative of the values near the extrema at the element boundary than the quadrature  
168 point value. The relationship between the nodal values, the basis functions and the proposed  
169 control volumes is illustrated schematically in one-dimension in parts (f) and (i) in Figure 2.

### 170 3. Methods

171 Here we focus on CAM-SE, however, in principle the methods apply to any element-based high-  
172 order Galerkin model. The physics grid in CAM-SE is defined by sub-dividing each element using  
173 equi-angular gnomonic coordinate lines to define the sides of the physics grid control volumes (see  
174 the Appendix for details). Note that the element boundaries are defined by equi-angular gnomonic  
175 grid lines. The notation  $pg = 3$  refers to the configuration where the elements are divided into  
176  $pg \times pg = 3 \times 3$  equi-angular physics grid cells (see Figure 5) resulting in a quasi-equal spherical  
177 area grid resembling the cubed-sphere. Defining the physics grid by sub-dividing elements makes  
178 it possible to use the same element infrastructure as already used in CAM-SE, thereby facilitating  
179 its implementation. Here we make use of the  $ne30np4$  and  $ne30pg3$  grids that use GLL quadrature  
180 point physics grid (physics and dynamics grid coincide), and the same ( $pg = 3$ ) resolution quasi

181 equal-area physics grids, respectively. In all configurations we use degree three Lagrange basis  
182 ( $np = 4$ ) and  $ne \times ne = 30 \times 30$  elements on each cubed-sphere panel.

183 A consequence of separating physics and dynamics grids is that the atmospheric state must be  
184 mapped to the physics grid and the physics tendencies must be mapped back to the dynamics  
185 grid. This is discussed in separate sections below. When separating physics and dynamics grids it  
186 is advantageous to use a vertical coordinate that is static during physics-dynamics coupling. This  
187 was one motivation to switch to a dry-mass vertical coordinate in CAM-SE (Lauritzen et al. 2018);  
188 since dry mass remains constant throughout physics the dry-mass vertical coordinate remains fixed  
189 during physics-dynamics coupling. The dry mass coordinate subsequently evolves as floating  
190 Lagrangian layers by the dynamics (Lin 2004) periodically mapped back to a reference hybrid-  
191 sigma-pressure coordinate after Simmons and Burridge (1981). All variables mapped between  
192 grids are collocated, layer-mean values (Lauritzen et al. 2018).

193 a. *Mapping state from dynamics grid (GLL) to physics grid (pg)*

194 The dynamics state is defined on the GLL grid in terms of temperature  $T^{(gll)}$ , zonal wind com-  
195 ponent  $u^{(gll)}$ , meridional wind component  $v^{(gll)}$ , and dry pressure level thickness  $\Delta p^{(gll)}$ . In the  
196 mapping of the atmospheric state to the physics grid it is important that the following properties  
197 are met:

- 198 1. conservation of scalar quantities such as mass and dry thermal energy,
- 199 2. for tracers; shape-preservation (monotonicity), i.e., the mapping method must not introduce  
200 new extrema in the interpolated field, in particular, negatives,
- 201 3. consistency, i.e., the mapping preserves a constant,

202     4. linear correlation preservation, i.e., if field A is a linear function of B, this relationship is still  
 203       preserved (see, e.g, equation 5 in Lauritzen and Thuburn 2012)

204     Other properties that may be important, but not pursued here, includes total energy conservation  
 205     and axial angular momentum conservation. Total energy is a quadratic quantity that is inherently  
 206     difficult to conserve unless one maps total energy requiring one to diagnose either temperature or  
 207     momentum components. For example, enforcing total energy conservation locally using, e.g., Lin  
 208     (2004)'s method where total energy and velocity components are remapped and temperature is a  
 209     derived variable, has proven problematic (C. Chen, personal communication). Similarly conserva-  
 210     tion of axial angular momentum is problematic. Conservation of angular momentum requires one  
 211     to interpolate the zonal and meridional components of momentum which creates large errors near  
 212     the poles. To avoid the pole problem we interpolate contra-variant components of the momentum  
 213     vector, which violates axial angular momentum conservation.

214     We argue that the most consistent method for mapping scalar state variables from the GLL grid  
 215     to the physics grid is to integrate the Lagrange basis function representation (used by the SE dy-  
 216     namical core) over the physics grid control volumes, i.e., integrate the basis function representation  
 217     of  $\Delta p^{(gll)} \times T^{(gll)}$  and  $\Delta p^{(gll)}$  over the physics grid control volume (see, e.g., Lauritzen et al. 2017;  
 218     Ullrich and Taylor 2015)

$$\Delta p^{(pg)} = \frac{1}{A^{(pg)}} \int_{A^{(pg)}} \Delta p^{(gll)} dA, \quad (1)$$

$$T^{(pg)} = \frac{1}{A^{(pg)} \Delta p^{(pg)}} \int_{A^{(pg)}} T^{(gll)} \Delta p^{(gll)} dA, \quad (2)$$

219     where  $A^{(pg)}$  is the physics grid area. The integrals are numerically computed using the GLL  
 220     quadrature rule on each physics grid element, which exactly (to machine precision) integrates the  
 221     basis functions over the  $pg$  control volumes (Lauritzen et al. 2017). Thermal energy and dry air  
 222     mass is conserved and the mapping is consistent. For the wind, which is a vector, the zonal and

223 meridional wind components are mapped by transforming to contra-variant wind components,  
224 evaluating the basis function representation thereof at the equi-angular center of the physics grid  
225 control volumes and then transformed back to latitude-longitude coordinate system winds. All of  
226 the operations are local to the element and do not require communication between elements.

227 The mapping of tracers is more problematic since the SE basis function representation is oscil-  
228 latory although the shape-preserving filter guarantees shape-preservation at the GLL nodes (Guba  
229 et al. 2014a). To avoid this issue we use the CAM-SE-CSLAM version of CAM-SE (Conservative  
230 Semi-Lagrangian Multi-tracer transport scheme Lauritzen et al. 2017), where tracers are advected  
231 on the  $pg = 3$  physics grid using the inherently mass and linear-correlation preserving CSLAM al-  
232 gorithm. Note that in CAM-SE-CSLAM the dry mass internally predicted by CSLAM,  $\Delta p^{(cslam)}$ ,  
233 is, by design, equal to  $\Delta p^{(gll)}$  integrated over the CSLAM/physics grid control volume (Lauritzen  
234 et al. 2017). Since the tracer grid and physics grids are co-located and  $\Delta p^{(pg)} = \Delta p^{(cslam)}$  then the  
235 mass conservation, correlation preservation, consistency and shape-preservation constraints are  
236 inherently fulfilled.

237 *b. Mapping tendencies from physics grid (pg) to dynamics grid (GLL)*

238 The physics tendencies are computed on the finite-volume physics grid and are denoted  
239  $f_T^{(pg)}, f_u^{(pg)}, f_v^{(pg)}$ , and  $f_m^{(pg)}$ . Note that dry air mass is not modified by physics and hence there  
240 is no tendency for dry mass,  $f_{\Delta p} \equiv 0$ . Also, it is important to map tendencies and not state from  
241 the physics grid to GLL grid otherwise one will get spurious tendencies from mapping errors when  
242 the actual physics tendency is zero (unless a reversible map is used).

243 It is important that this process:

- 244 1. for tracers; mass tendency is conserved,

- 245 2. for tracers; in each tracer grid cell the mass tendency from physics must not exceed tracer  
246 mass available in tracer grid cell (it is assumed that the physics tendency will not drive tracer  
247 mixing ratio negative on the physics grid),  
  
248 3. linear correlation preservation,  
  
249 4. consistency, i.e., the mapping preserves a constant tendency.

250 Other properties that may be important, but not pursued here, includes total energy conservation  
251 (incl. components of total energy) and axial angular momentum conservation. Scalar variables  
252 are mapped from the physics grid to GLL grid using a tensor-product Lagrange interpolation in  
253 two dimensions (i.e., we assume that the pressure variations in the vertical are small). The local  
254 coordinates on a cubed-sphere are discontinuous at the element edges so the interpolation requires  
255 special attention at the cube corners and edges. The details are provided in the Appendix. Lagrange  
256 interpolation preserves a constant (including zero) and linear correlations. Tracer and physics grids  
257 are co-located so tracer mass, tracer shape, and tracer correlations are trivially preserved on the  
258 tracer grid; and the inconsistency in point 2 above will not appear.

259 Mapping from  $pg$  to GLL grids while conserving mass was found to be difficult without ex-  
260 cessive grid imprinting at element edges. Mass-conservation (using conventional finite-volume  
261 methods) requires a control volume to be defined around the GLL points (see Figure 4 in this  
262 paper or Figure 8b in Ullrich et al. 2016). These volumes are artificial and not consistent with  
263 the SE method. Integrating the CSLAM reconstruction of water tracers of such artificial control  
264 volumes led to GLL node grid imprinting in the mapping and will not preserve a constant mixing  
265 ratio since the mapping of  $\Delta p^{(pg)}$  to GLL will not yield the GLL node value for dry pressure-level  
266 thickness (i.e., the maps are not reversible). A reversible map requires that the number of degrees  
267 of freedom on the source mesh ( $pg3$  has 9 degrees of freedom) equal the number of degrees of

268 freedom on the target mesh ( $np4$  grid has 16 degrees of freedom). This condition is violated by  
269 construction for individual elements.

270 It was also found important to use an interpolator that is smooth across element boundaries.

271 Using an algorithm that only uses information from an element or control volumes will (at best)  
272 be  $C^0$  at the element boundaries and therefore lead to boundary node grid imprinting. A stencil that  
273 extends beyond one element is therefore necessary. After much experimentation, the best results  
274 in terms of grid-imprinting were obtained with tensor-cubic interpolation (see the Appendix for  
275 details) and by using the CAM-SE-CSLAM configuration (which requires the same boundary  
276 exchange/communication as used in CSLAM).

277 *c. Time splitting and physics-dynamics coupling*

278 The physics and dynamics are integrated in time using a sequential-update approach (e.g.,  
279 Williamson 2002). The dynamical core is sub-cycled over the (usually) longer physics time-step,  
280  $\Delta t_{phys}$ , e.g., the vertical remapping time-step  $\Delta t_{remap}$  is cycled  $nsplit$  times, totaling to  $\Delta t_{phys}$ . In  
281 CAM-SE, a fraction of the physics forcing, e.g.,  $f_q \times \Delta t_{remap}$  is applied at the beginning of each  
282  $nsplit$  vertical remap subcycles, such that the full forcing ( $f_q \times \Delta t_{phys}$ ) is realized over the course  
283 of a physics time-step. This approach of dribbling the tendencies over sub-intervals has the ad-  
284 vantage of reducing gravity wave noise (Thatcher and Jablonowski 2016), but may disrupt tracer  
285 mass conservation (Zhang et al. 2017). In CAM-SE-CSLAM, all but the tracer mass quantities are  
286 dribbled, with tracer mass receiving the full physics update, e.g.,  $f_q \times \Delta t_{phys}$ , applied only at the  
287 beginning of the first remap sub-cycle, and thereby conserving tracer mass. This is the  $ftype = 2$   
288 configuration described in detail in Section 3.6.3 in Lauritzen et al. (2018).

289 In the SE integration of the equations of motion on the GLL grid the water species are  
290 needed in the computation of the pressure gradient force and generalized expressions for heat

capacity at constant pressure  $c_p$ , etc. Hence the mixing ratios for water vapor and dynamically/thermodynamically active condensates (e.g., cloud liquid and cloud ice) are needed on the GLL grid. We have chosen to advect the water species on the GLL grid using the SE method as well as on the physics grid using CSLAM. Every time physics updates the water species on the CSLAM grid, a forcing term (equal to the difference between updated CSLAM water variables and the SE values) is applied to the GLL water variables using dribbling so that the CSLAM solution and SE solution for water species are tightly coupled.

## 4. Results

A hierarchy of idealized model configurations are presented in order to elucidate the differences between CAM-SE and CAM-SE-CSLAM (available from the CESM2.1 release; <https://doi.org/10.5065/D67H1H0V>). Here, the configurations are presented in order of increasing complexity, each with a pair of approximately  $1^\circ$  simulations, pertaining to the *ne30np4* (CAM-SE) and *ne30pg3* (CAM-SE-CSLAM) grids, and a  $\Delta t_{phys} = 1800$  s.

### a. Moist Baroclinic Wave

The moist baroclinic wave test case was developed as part of the ‘CESM Simple Models’ project (Polvani et al. 2017), and included in the release of CESM2. It is effectively the dry test-case of Ullrich et al. (2014), but initialized with moisture and coupled to the Kessler moist physics routine (Kessler 1969). For more details on this test case (which was part of the 2016 Dynamical Core Model Intercomparison Project, Ullrich et al. 2017), see Section 4.1 in Lauritzen et al. (2018). A measure of the uncertainty in the reference solution, the  $L_2$  difference norm between two high-resolution solutions using different dynamical cores, was also presented in Lauritzen et al. (2018)

312 and provided again here in Figure 6. The  $L_2$  norm between CAM-SE and CAM-SE-CSLAM lies  
313 below the uncertainty of the reference solution, indicating their differences are insignificant.

314 The flow field of the baroclinic wave test is used to drive the terminator “toy”-chemistry test of  
315 Lauritzen et al. (2015b, 2017). The terminator test is used to assess linear-correlation preservation  
316 using two reactive species advected across the terminator line. The model is initialized with species  
317 for which their weighted sum,  $Cl_y$ , is a constant (constant surface pressure and constant mixing  
318 ratio;  $Cl_y = Cl + 2Cl_2 = 4 \times 10^{-6} \text{ kg/kg}$ ), such that if tracer correlations are preserved, then the  
319 column-integrated weighted sum of the species should not vary in time. Figure 7 provides a  
320 snapshot of the vertically integrated weighted sum of species at day 15. In CAM-SE, the tracer  
321 correlations are not preserved at day 15 and the field is populated by overshoots and undershoots.  
322 In contrast, by day 15, CAM-SE-CSLAM still conserves tracer correlations to within machine  
323 precision, consistent with the previous results of this test-case initialized with a dry baroclinic  
324 wave (Lauritzen et al. 2017).

### 325 b. *Aqua-planets*

326 Two year long aqua-planet simulations are performed using CAM-SE and CAM-SE-CSLAM,  
327 using the CAM4 physics package (Neale et al. 2010), as discussed in Section 2. Away from the  
328 grid-scale, the mean states in the two models are very similar. Figure 8 shows the zonal-mean cli-  
329 matological precipitation rates in CAM-SE and CAM-SE-CSLAM. Considering how sensitive this  
330 aqua-planet configuration is to design choices in CAM-SE (Lauritzen et al. 2018), it is somewhat  
331 unexpected that the zonal means look so similar to one another.

332 A plot similar to Figure 3a is constructed for the CAM-SE-CSLAM simulation, a probability  
333 density distribution of upward  $\omega$  conditionally sampled based on location within the element. Like  
334 Figure 3a, Figure 3b divides up the control volumes by corner, edge and interior cells. Through the

335 use of the quasi-equal area physics grid, the dynamical core state appears more or less independent  
336 of location within the element, a marked improvement over CAM-SE. Since the state is approxi-  
337 mately independent of in-element location, it follows that the physics forcing, which is evaluated  
338 from the dynamical core state, may be expected to also show an improvement in grid-imprinting.

339 The low-level, mean and variance of the temperature tendencies from the physics, on the GLL  
340 grid,  $f_T^{(gll)}$ , in the two simulations are shown in Figure 9. The mean states in the two models  
341 resemble one another, consistent with the zonal mean precipitation rates (Figure 8). The mean  
342 physics tendencies contains modest grid imprinting in CAM-SE (barely visible near the storm-  
343 track regions), while in the variance field, grid imprinting is both ubiquitous and unmistakable.  
344 The variance is larger on boundary nodes, manifesting as a ‘stitching’ pattern resembling the  
345 cube-sphere grid. In CAM-SE-CSLAM, the grid imprinting is all but eliminated based on the  
346 mean and variance of the physics tendencies (Figure 9), consistent with our expectation.

347 The global mean and variance of the low-level physics tendencies are slightly lower in *pg3* com-  
348 pared with *np4*, on the GLL grid (by about 1% and 6% for the mean and variance, respectively;  
349 Figure 9). Through re-creating Figure 3a, but using the  $\omega$  field on the GLL grid in the *pg3* sim-  
350 ulations, the frequency of large magnitude  $\omega$  values (less than -1.0 Pa/s) associated with interior,  
351 corner and edge nodes are slightly lower (not shown). This suggests that the lower magnitude  
352 physics forcing in *pg3* impacts the state on the GLL grid, albeit modestly. Therefore the lower fre-  
353 quency of large magnitude  $\omega$  in the *pg3* run (Figure 3) is not solely due to the smoothing effect of  
354 integrating the basis functions over control volumes, but also a result of lower magnitude physics  
355 tendencies feeding back onto the dynamical state.

356 As stated in Section 3, the mapping of the state to the physics grid and the reverse interpolation  
357 of physics tendencies to the GLL grid is not total energy conserving. CAM has a global energy  
358 fixer (Williamson et al. 2015) which can be used to estimate the errors associated with the mapping

algorithms. To do so, it is presumed that there are no compensating mapping errors in going to and from the physics and dynamics grids, and that CAM-SE-CSLAM and CAM-SE have the same energy dissipation rates. Under these assumptions the spurious globally integrated total energy errors due to the mapping algorithm is estimated to be approximately  $0.0025 \text{ W/m}^2$  in the aqua-planet simulations. In comparison, the dynamical core total energy dissipation is on the order of  $0.1 \text{ W/m}^2$  (Lauritzen et al. 2018).

### 365 c. Held-Suarez with Topography

366 Grid imprinting associated with the flow around obstacles is more problematic than that en-  
367 countered on the aqua-planets. In order to diagnose grid imprinting due to topographic flow, an  
368 idealized Held-Suarez configuration (Held and Suarez 1994) is outfitted with real world topogra-  
369 phy after Fox-Rabinovitz et al. (2000); Baer et al. (2006), and run for two years. Figure 10 shows  
370 the mean  $\omega$  at two different vertical levels in the middle troposphere. The data are presented as a  
371 raster plot on their respective unstructured grids, in order to delineate whether a particular value is  
372 associated with an interior, edge or element boundary node.

373 At higher latitudes (e.g., the southern Andes), the flow is smooth, conforming reasonably to  
374 the underlying topography. At lower latitudes, over the Andes (**between the equator and  $20^\circ\text{S}$** )  
375 or the Himalayas (**from  $20^\circ\text{N}$  to  $30^\circ\text{N}$** ), there is a clear preference for extrema to occur at the  
376 element boundaries (Figure 10). The vertical structure of  $\omega$  in regions of strong grid-imprinting  
377 indicates full-troposphere upward/downward motion (not shown). Grid imprinting is therefore  
378 more common in regions of weak stratification, such as occurs in the deep tropics, with forced up-  
379 slope flow facilitating the release of gravitational instability. Resolved updrafts/downdrafts often  
380 align with the element boundaries due to its systematically tighter pressure gradients.

381 Through the use of the quasi-equal area physics grid, grid imprinting due to topographic flow  
382 is reduced (Figures 10). The native topography lives on the physics grid, and the topography is  
383 mapped to the nodal points at run-time in CAM-SE-CSLAM. Mapping topography to the quadra-  
384 ture nodes ensures that no new extrema will be introduced to the boundary nodes, where the  
385 solution is least smooth. This effect can not be very large, since the grid noise is similar in CAM-  
386 SE and CAM-SE-CSLAM on the GLL grid (**not shown**). From the perspective of the physics  
387 grid, the CAM-SE-CSLAM solution clearly mitigates the influence of grid-induced extrema on  
388 the state. **This can be seen by comparing Figures 10a and 10b, and their differences (Figure 10c).**  
389 The reduction in grid imprinting in this modified Held-Suarez configuration appears to be almost  
390 entirely a result of the smoothing effect of integrating the basis functions over the control volumes  
391 of the physics grid.

#### 392 *d. AMIP type simulations*

393 A pair of 20 year-long AMIP type simulations are performed, using CAM, version 6 physics  
394 package (CAM6) and using perpetual year 2000 SST boundary conditions (*F2000climo* compset  
395 in CESM2.0; <https://doi.org/10.5065/D67H1H0V>). Figure 11 shows the climatological pre-  
396 cipitation fields in CAM-SE (left) and CAM-SE-CSLAM (middle), and over the same mountain-  
397 ous regions as in Figure 10. The plots have some similar features to the  $\omega$  field in the Held-Suarez  
398 runs; the greater variance at lower latitudes, and on the windward side of the mountains are broadly  
399 similar. CAM-SE-CSLAM has a lower spatial variance, e.g., the lack of extrema over the Andes  
400 at about 15° S compared to CAM-SE, and the grid-scale precipitation peak over the Himalayas  
401 at about 30° N. The difference plot (Figure 11; right panel) is more broadly populated by blue,  
402 purple and white contours, indicating that CAM-SE has, in general, larger magnitude precipitation  
403 rates over high topography. The difference plots also highlight a couple of zonally aligned strips

404 of anomalous precipitation, in particular, near the foot of the Himalayas in CAM-SE. These bands  
405 are in the same location as the bands of precipitation identified in CAM-SE in Lauritzen et al.  
406 (2015a) (their Figure 7), but using CAM, version 5 physics, of which they argue are spurious in  
407 nature.

408 To assist in identifying whether a particular precipitation pattern is spurious, an *F2000climo*  
409 simulation is carried out using the finite-volume dynamical core that uses a regular latitude-  
410 longitude  $0.9^\circ \times 1.25^\circ$  grid (CAM-FV; *f09* grid; Neale et al. 2012). CAM-FV is the default  
411 low resolution model in CESM2.0, and with its smoothly varying grid, does not suffer from the  
412 Quadrature Node Problem (Section 2). Figure 12 shows the global precipitation fields in CAM-SE,  
413 CAM-SE-CSLAM and CAM-FV, compared to an observational dataset, the Global Precipitation  
414 Climatology Project (GPCP; 1979-2003) gridded dataset (Huffman et al. 2001). The magnitude  
415 of the precipitation rates in all three models are higher than the GPCP dataset, primarily over land  
416 in the Tropics (note the lack of red contours in the GPCP dataset), which should be interpreted  
417 cautiously due to widely-accepted issues in constructing a reliable, gridded, global precipitation  
418 dataset. At lower latitudes, CAM-FV has lower spatial variance, and overall lower magnitudes,  
419 compared with CAM-SE. The GPCP dataset indicates that perhaps the precipitation rates in low-  
420 latitude mountainous regions in CAM-FV and CAM-SE are larger than in reality. Following suit,  
421 the reduction in magnitude and spatial variance in precipitation in these regions in CAM-SE-  
422 CSLAM may be interpreted as an improvement over CAM-SE.

## 423 5. Conclusions

424 Element-based high-order Galerkin Methods possess many of the attractive qualities recom-  
425 mended for next generation global atmospheric models. Among these, high-order accuracy is  
426 achieved with minimal communication between elements, allowing for near perfect scaling on

massively parallel systems. Element communication amounts to a numerical flux applied to the element boundaries, reconciling overlapping solutions of adjacent elements but degrading the smoothness of the boundary nodes in the process (to  $C^0$ ). For non-smooth problems, gradients are systematically tighter at the element boundaries, and local extrema often characterize the boundary nodes. This behavior is illustrated using NCAR's Community Atmosphere Model with Spectral Elements dynamics (CAM-SE) in an aqua-planet configuration, in a Held-Suarez configuration with real-world topography and in an AMIP type configuration.

The authors argue that the conventional physics-dynamics coupling paradigm, in which the physical parameterizations are evaluated on the dynamical core grid, exacerbates grid imprinting. A separate physics grid is proposed and implemented in CAM-SE, and referred to as CAM-SE-CSLAM, through dividing the elements into quasi-equal areas with equivalent degrees of freedom. The state is mapped to the physics grid with high-order accuracy through integrating CAM-SE's Lagrange basis functions over the control volumes. Control volumes near element boundaries now represent a state in the vicinity of the extrema produced through the boundary exchange, as opposed to the nodal value itself. These control volumes are also compatible with a 'large-scale state' as required by the physical parameterizations. The physical parameterizations are evaluated on the finite volume grid, and the forcing terms are mapped back to the dynamical core grid using a cubic tensor-product Lagrange interpolation. In aqua-planet simulations, evaluating the parameterizations on the physics grid removes any obvious dependence of proximity to the element boundary, resulting in a more realistic state with negligible grid imprinting. The mapping algorithm does not conserve total energy, but it is estimated that these errors are one to two orders of magnitude less than the total energy dissipation from the dynamical core.

In CAM-SE-CSLAM, the physics grid replaces the default CAM-SE quadrature point-based coupler grid (Figure 4) to compute fluxes between model components in the Community Earth

451 System Model (CESM). The appeal here is two-fold. Through integrating the Lagrange basis  
452 functions over control volumes, one can be certain that the fluxes computed from this grid are a  
453 volume averaged flux. The same can not be said for CAM-SE, where artificial control volumes  
454 (with sizes proportional quadrature weights) are constructed around nodal values and assumed to  
455 represent the volume averaged state. The second advantage of the new coupler grid is that extrema  
456 occurring on boundary nodes may no longer influence other model components in simulations  
457 without rough topography. While grid imprinting is effectively eliminated in the aqua-planets,  
458 experiments with real-world topography (Held-Suarez and AMIP type configurations) reduces,  
459 but does not entirely eliminate, imprinting from the mean state. The quasi-equal area physics grid  
460 is nonetheless effective at mitigating numerical nuances associated with high-order element-based  
461 Galerkin methods, for non-smooth problems.

462 Future work will focus on the impact of using a coarser,  $pg \times pg = 2 \times 2$  physics grid configu-  
463 ration. The coarser physics grid may be more effective at reducing spurious noise over regions of  
464 rough topography, while potentially reducing the computational overhead. Any advantages of us-  
465 ing a coarser resolution physics grid will be weighed against any potential reduction in a model's  
466 effective resolution.

467 *Acknowledgments.* NCAR is sponsored by the National Science Foundation (NSF). We thank  
468 three anonymous reviewers for their helpful comments that significantly improved the clarity of  
469 the manuscript. Herrington thanks NCAR's Computational and Information Systems Laboratory  
470 (CISL) and NCAR's Climate and Global Dynamics division (CGD) for computational resources  
471 and technical support. Herrington, Reed, and Lauritzen are grateful to the NCAR Advanced Study  
472 Program graduate visitor program for funding Herrington's 12-month visit. Goldhaber was par-  
473 tially supported by the Accelerated Climate Modeling for Energy (ACME) project, and work pack-

474 age 12 – 015334 “Multiscale Methods for Accurate, Efficient, and the Accelerated Scale-Aware  
 475 Models, both funded through the U.S. Department of Energy Office of Biological and Environ-  
 476 mental Research. Goldhaber is also partially supported through NSF award AGS-1500187 “De-  
 477 velopment and Testing of a Global Quasi 3-D multi Modeling Framework.” Model source code is  
 478 officially released with CESM2.1 (<https://doi.org/10.5065/D67H1H0V>).

## 479 APPENDIX

480 The mapping of the physics tendencies from the physics grid to the GLL grid is done with  
 481 tensor-cubic Lagrange interpolation. The elements of the cubed-sphere in SE are created  
 482 from an equi-angular gnomonic projection. Consider one element  $(\alpha, \beta) \in [\alpha_1^{(elem)}, \alpha_2^{(elem)}] \times$   
 483  $[\beta_1^{(elem)}, \beta_2^{(elem)}]$ , where  $(\alpha, \beta)$  are central angle coordinates and  $\alpha_1^{(elem)}$  and  $\alpha_2^{(elem)}$  are the min-  
 484 imum and maximum central angles in the  $\alpha$ -coordinate direction, respectively, and similarly for  
 485  $\beta$ . Let  $\Delta\alpha^{(elem)} = \alpha_2^{(elem)} - \alpha_1^{(elem)}$  and  $\Delta\beta^{(elem)} = \beta_2^{(elem)} - \beta_1^{(elem)}$ . The physics grid cell central  
 486 angle centers are located at

$$(\alpha_i^{(pg)}, \beta_j^{(pg)}) = \left[ \alpha_1^{(elem)} + (i - \frac{1}{2}) \Delta\alpha^{(pg)}, \beta_1^{(elem)} + (j - \frac{1}{2}) \Delta\beta^{(pg)} \right], \quad (\text{A1})$$

487 where  $\Delta\alpha^{(pg)} = \Delta\beta^{(pg)} = \frac{\Delta\alpha^{(elem)}}{pg} = \frac{\Delta\beta^{(elem)}}{pg}$ . The interpolation is performed in central-angle co-  
 488 ordinates using tensor product cubic interpolation. For elements located on a cubed-sphere edge  
 489 or corner the coordinate system for neighboring elements may be on a different panel. To take  
 490 into account this coordinate change the central angle locations of physics grid cell centers located  
 491 on other panels are transformed to the coordinate system of the panel the element in question is  
 492 located on (the transformations are given in, e.g., Nair et al. 2005). An illustration is given in  
 493 Figure A1 for an element located in the lower left corner of a panel. The element in question is

494  $(\xi, \chi) \in (-1, 1)^2$  where, for simplicity, we have transformed the element coordinates into normal-  
 495 ized coordinates  $(\xi, \chi) = \left( \frac{2(\alpha^{(pg)} - \alpha_1^{(elem)})}{\Delta\alpha^{(elem)}} - 1, \frac{2(\beta^{(pg)} - \beta_1^{(elem)})}{\Delta\beta^{(elem)}} - 1 \right)$ ; also used internally in the  
 496 SE dynamical core (see, e.g., section 3.3 in Lauritzen et al. 2018). The GLL points are located at  
 497  $-1, -1/\sqrt{1}, 1/\sqrt{5}$ , and 1 in each coordinate direction. Near the edges/corners of an element cubic  
 498 extrapolation is used if the centered stencil expands beyond the panel.

## 499 References

- 500 Arakawa, A., and W. H. Schubert, 1974: Interaction of a cumulus cloud ensemble with the large-  
 501 scale environment, Part I. *J. Atmos. Sci.*, **31**, 674–701.
- 502 Bacmeister, J. T., K. A. Reed, C. Hannay, P. Lawrence, S. Bates, J. E. Truesdale, N. Rosen-  
 503 bloom, and M. Levy, 2018: Projected changes in tropical cyclone activity under future warm-  
 504 ing scenarios using a high-resolution climate model. *Climatic Change*, **146**, 547–560, doi:  
 505 10.1007/s10584-016-1750-x, URL <http://dx.doi.org/10.1007/s10584-016-1750-x>.
- 506 Baer, F., H. Wang, J. J. Tribbia, and A. Fournier, 2006: Climate modeling with spectral elements.  
 507 *Mon. Wea. Rev.*, **134**, 3610–3624, doi:10.1175/MWR3360.1, URL <http://dx.doi.org/10.1175/MWR3360.1>.
- 508 Brdar, S., M. Baldauf, A. Dedner, and R. Klöfkorn, 2013: Comparison of dynamical cores for  
 509 nwp models: comparison of cosmo and dune. *Theoretical and Computational Fluid Dynamics*,  
 510 **27 (3-4)**, 453–472, doi:10.1007/s00162-012-0264-z.
- 512 Canuto, C., M. Y. Hussaini, A. Quarteroni, and T. Zang, 2007: *Spectral Methods: Evolution to*  
 513 *Complex Geometries and Applications to Fluid Dynamics*. 1st ed., Springer.
- 514 Dennis, J. M., and Coauthors, 2012: CAM-SE: A scalable spectral element dynamical core for  
 515 the Community Atmosphere Model. *Int. J. High. Perform. C.*, **26 (1)**, 74–89, doi:10.1177/

- 516 1094342011428142, URL <http://hpc.sagepub.com/content/26/1/74.abstract>, <http://hpc.sagepub.com/content/26/1/74.full.pdf+html>.
- 517
- 518 Durran, D., 2010: *Numerical Methods for Fluid Dynamics: With Applications to Geophysics*,  
519 Texts in Applied Mathematics, Vol. 32. 2nd ed., Springer, 516 p.
- 520 Fournier, A., M. A. Taylor, and J. J. Tribbia, 2004: The spectral element atmosphere model  
521 (SEAM): High-resolution parallel computation and localized resolution of regional dynamics.  
522 *Mon. Wea. Rev.*, **132** (3), 726–748.
- 523 Fox-Rabinovitz, M. S., G. L. Stenchikov, M. J. Suarez, L. L. Takacs, and R. C. Govindaraju, 2000:  
524 A uniform- and variable-resolution stretched-grid gcm dynamical core with realistic orography.  
525 *Mon. Wea. Rev.*, **128**, 1883–1898.
- 526 Giraldo, F., and M. Restelli, 2008: A study of spectral element and discontinuous galerkin methods  
527 for the Navier-Stokes equations in nonhydrostatic mesoscale atmospheric modeling: Equation  
528 sets and test cases. *J. Comput. Phys.*, **227** (8), 3849 – 3877, doi:<http://dx.doi.org/10.1016/j.jcp.2007.12.009>.
- 529
- 530 Guba, O., M. Taylor, and A. St-Cyr, 2014a: Optimization-based limiters for the spectral element  
531 method. *J. Comput. Phys.*, **267** (0), 176 – 195, doi:<http://dx.doi.org/10.1016/j.jcp.2014.02.029>.
- 532 Guba, O., M. A. Taylor, P. A. Ullrich, J. R. Overfelt, and M. N. Levy, 2014b: The spectral element  
533 method (sem) on variable-resolution grids: evaluating grid sensitivity and resolution-aware nu-  
534 matical viscosity. *Geosci. Model Dev.*, **7** (6), 2803–2816, doi:[10.5194/gmd-7-2803-2014](https://doi.org/10.5194/gmd-7-2803-2014).
- 535 Held, I. M., and M. J. Suarez, 1994: A proposal for the intercomparison of the dynamical cores of  
536 atmospheric general circulation models. *Bull. Am. Meteorol. Soc.*, **73**, 1825–1830.

- 537 Huffman, G. J., R. F. Adler, M. M. Morrissey, D. T. Bolvin, S. Curtis, R. Joyce, B. McGavock,  
538 and J. Susskind, 2001: Global precipitation at one-degree daily resolution from multisatellite  
539 observations. *J. Hydrometeorology*, **2** (1), 36–50.
- 540 Kessler, E., 1969: On the distribution and continuity of water substance in atmospheric circula-  
541 tions. *Meteorol. Monogr.*, **10** (32), 88.
- 542 Kim, Y.-J., F. X. Giraldo, M. Flatau, C.-S. Liou, and M. S. Peng, 2008: A sensitivity study of the  
543 kelvin wave and the Madden-Julian oscillation in aquaplanet simulations by the Naval Research  
544 Laboratory Spectral Element Atmospheric Model. *J. Geo. Res.: Atmospheres*, **113** (D20), doi:  
545 10.1029/2008JD009887, d20102.
- 546 Lander, J., and B. Hoskins, 1997: Believable scales and parameterizations in a spectral transform  
547 model. *Mon. Wea. Rev.*, **125**, 292–303., doi:10.1175/1520-0493.
- 548 Lauritzen, P., and J. Thuburn, 2012: Evaluating advection/transport schemes using interrelated  
549 tracers, scatter plots and numerical mixing diagnostics. *Quart. J. Roy. Met. Soc.*, **138** (665),  
550 906–918, doi:10.1002/qj.986.
- 551 Lauritzen, P. H., J. T. Bacmeister, P. F. Callaghan, and M. A. Taylor, 2015a: Ncar global model  
552 topography generation software for unstructured grids. *Geoscientific Model Development Dis-*  
553 *cussions*, **8** (6), 4623–4651, doi:10.5194/gmdd-8-4623-2015.
- 554 Lauritzen, P. H., A. J. Conley, J.-F. Lamarque, F. Vitt, and M. A. Taylor, 2015b: The terminator  
555 “toy” chemistry test: a simple tool to assess errors in transport schemes. *Geoscientific Model  
556 Development*, **8** (5), 1299–1313, doi:10.5194/gmd-8-1299-2015.
- 557 Lauritzen, P. H., M. A. Taylor, J. Overfelt, P. A. Ullrich, R. D. Nair, S. Goldhaber, and  
558 R. Kelly, 2017: CAM-SE-CSLAM: Consistent coupling of a conservative semi-lagrangian

- finite-volume method with spectral element dynamics. *Mon. Wea. Rev.*, **145** (3), 833–855, doi: 10.1175/MWR-D-16-0258.1.
- Lauritzen, P. H., and Coauthors, 2018: NCAR CESM2.0 release of CAM-SE: A reformulation of the spectral-element dynamical core in dry-mass vertical coordinates with comprehensive treatment of condensates and energy. *J. Adv. Model. Earth Syst.*, doi:10.1029/2017MS001257.
- Lin, S.-J., 2004: A 'vertically Lagrangian' finite-volume dynamical core for global models. *Mon. Wea. Rev.*, **132**, 2293–2307.
- Maday, Y., and A. T. Patera, 1987: Spectral element methods for the incompressible Navier Stokes equations. *State of the Art Surveys on Computational Mechanics*, A. K. Noor, and J. T. Oden, Eds., ASME, New York, 71–143.
- Medeiros, B., D. L. Williamson, and J. G. Olson, 2016: Reference aquaplanet climate in the community atmosphere model, version 5. *J. Adv. Model. Earth Syst.*, **8** (1), 406–424, doi:10.1002/2015MS000593.
- Nair, R., H.-W. Choi, and H. Tufo, 2009: Computational aspects of a scalable high-order discontinuous galerkin atmospheric dynamical core. *Computers & Fluids*, **38** (2), 309 – 319, doi: <http://dx.doi.org/10.1016/j.compfluid.2008.04.006>.
- Nair, R. D., M. N. Levy, and P. H. Lauritzen, 2011: Emerging numerical methods for atmospheric modeling, in: P.H. Lauritzen, R.D. Nair, C. Jablonowski, M. Taylor (Eds.), Numerical techniques for global atmospheric models. *Lecture Notes in Computational Science and Engineering*, Springer, **80**.
- Nair, R. D., S. J. Thomas, and R. D. Loft, 2005: A discontinuous galerkin transport scheme on the cubed sphere. *Mon. Wea. Rev.*, **133** (4), 814–828, doi:10.1175/MWR2890.1.

- 581 Neale, R. B., and B. J. Hoskins, 2000: A standard test for agcms including their physical  
582 parametrizations: I: the proposal. *Atmos. Sci. Lett.*, **1** (2), 101–107, doi:10.1006/asle.2000.0022.
- 583 Neale, R. B., and Coauthors, 2010: Description of the NCAR Community Atmosphere Model  
584 (CAM 4.0). NCAR Technical Note, National Center of Atmospheric Research.
- 585 Neale, R. B., and Coauthors, 2012: Description of the NCAR Community Atmosphere Model  
586 (CAM 5.0). NCAR Technical Note NCAR/TN-486+STR, National Center of Atmospheric Re-  
587 search.
- 588 Plant, R. S., and G. C. Craig, 2008: A stochastic parameterization for deep convection based  
589 on equilibrium statistics. *J. Atmos. Sci.*, **65**, 87–105, doi:10.1175/2007JAS2263.1, URL <http://dx.doi.org/10.1175/2007JAS2263.1>.
- 590 Polvani, L., A. Clement, B. Medeiros, J. Benedict, and I. Simpson, 2017: Opening the door to  
591 simpler climate models in the community earth system model project. *EOS*, submitted.
- 592 Putman, W. M., and S.-J. Lin, 2007: Finite-volume transport on various cubed-sphere grids. *J.*  
593 *Comput. Phys.*, **227** (1), 55–78.
- 594 Reed, K. A., J. T. Bacmeister, N. A. Rosenbloom, M. F. Wehner, S. C. Bates, P. H. Lauritzen,  
595 J. E. Truesdale, and C. Hannay, 2015: Impact of the dynamical core on the direct simulation  
596 of tropical cyclones in a high-resolution global model. *Geophys. Res. Lett.*, **42** (9), 3603–3608,  
597 doi:10.1002/2015GL063974.
- 598 Rhoades, A. M., X. Huang, P. A. Ullrich, and C. M. Zarzycki, 2016: Characterizing sierra  
599 nevada snowpack using variable-resolution cesm. *Journal of Applied Meteorology and Cli-*  
600 *matology*, **55** (1), 173–196, doi:10.1175/JAMC-D-15-0156.1, URL <https://doi.org/10.1175/JAMC-D-15-0156.1>.

- 603 Simmons, A. J., and D. M. Burridge, 1981: An energy and angular-momentum conserving vertical  
604 finite-difference scheme and hybrid vertical coordinates. *Mon. Wea. Rev.*, **109** (4), 758–766.
- 605 Small, R. J., and Coauthors, 2014: A new synoptic scale resolving global climate simulation  
606 using the community earth system model. *J. Adv. Model. Earth Syst.*, **6** (4), 1065–1094, doi:  
607 10.1002/2014MS000363.
- 608 Suarez, M. J., A. Arakawa, and D. A. Randall, 1983: The parameterization of the planetary  
609 boundary layer in the ucla general circulation model: Formulation and results. *Mon. Wea. Rev.*,  
610 **111** (11), 2224–2243.
- 611 Taylor, M., J. Edwards, and A. St-Cyr, 2008: Petascale atmospheric models for the community  
612 climate system model: new developments and evaluation of scalable dynamical cores. *J. Phys.:  
613 Conf. Ser.*, **125**, doi:10.1088/1742-6596/125/1/012023.
- 614 Taylor, M. A., and A. Fournier, 2010: A compatible and conservative spectral element method on  
615 unstructured grids. *J. Comput. Phys.*, **229** (17), 5879 – 5895, doi:10.1016/j.jcp.2010.04.008.
- 616 Thatcher, D. R., and C. Jablonowski, 2016: A moist aquaplanet variant of the Held–Suarez test  
617 for atmospheric model dynamical cores. *Geoscientific Model Development*, **9** (4), 1263–1292,  
618 doi:10.5194/gmd-9-1263-2016, URL <https://www.geosci-model-dev.net/9/1263/2016/>.
- 619 Ullrich, P. A., 2014: A global finite-element shallow-water model supporting continuous and dis-  
620 continuous elements. *Geosci. Model Dev.*, **7** (6), 3017–3035, doi:10.5194/gmd-7-3017-2014.
- 621 Ullrich, P. A., D. Devendran, and H. Johansen, 2016: Arbitrary-order conservative and consistent  
622 remapping and a theory of linear maps: Part ii. *Mon. Wea. Rev.*, **144** (4), 1529–1549, doi:  
623 10.1175/MWR-D-15-0301.1.

- 624 Ullrich, P. A., T. Melvin, C. Jablonowski, and A. Staniforth, 2014: A proposed baroclinic wave test  
625 case for deep and shallow-atmosphere dynamical cores. *Quart. J. Royal Meteor. Soc.*, **140** (682),  
626 1590–1602.
- 627 Ullrich, P. A., and M. A. Taylor, 2015: Arbitrary-order conservative and consistent remap-  
628 ping and a theory of linear maps: Part I. *Mon. Wea. Rev.*, **143**, 2419–2440, doi:10.1175/  
629 MWR-D-14-00343.1.
- 630 Ullrich, P. A., and Coauthors, 2017: "dcmip2016: A review of non-hydrostatic dynamical core  
631 design and intercomparison of participating models". *Geosci. Model Dev.*, **10**, 4477–4509, doi:  
632 10.5194/gmd-10-4477-2017.
- 633 Wan, H., and Coauthors, 2013: "the icon-1.2 hydrostatic atmospheric dynamical core on triangular  
634 grids, part i: formulation and performance of the baseline version". *Geosci. Model Dev.*, **6**, 735–  
635 763.
- 636 Wedi, N. P., 2014: Increasing horizontal resolution in numerical weather prediction and climate  
637 simulations: illusion or panacea? *Philosophical Transactions of the Royal Society of London A:*  
638 *Mathematical, Physical and Engineering Sciences*, **372** (2018), doi:10.1098/rsta.2013.0289.
- 639 Williamson, D. L., 1999: Convergence of atmospheric simulations with increasing horizontal res-  
640 olution and fixed forcing scales. *Tellus A*, **51**, 663–673, doi:10.1034/j.1600-0870.1999.00009.x.
- 641 Williamson, D. L., 2002: Time-split versus process-split coupling of parameterizations and dy-  
642 namical core. *Mon. Wea. Rev.*, **130**, 2024–2041.
- 643 Williamson, D. L., J. G. Olson, C. Hannay, T. Toniazzo, M. Taylor, and V. Yudin, 2015: Energy  
644 considerations in the community atmosphere model (cam). *J. Adv. Model. Earth Syst.*, **7** (3),  
645 1178–1188, doi:10.1002/2015MS000448, URL <http://dx.doi.org/10.1002/2015MS000448>.

- 646 Zarzycki, C. M., C. Jablonowski, and M. A. Taylor, 2014a: Using variable-resolution meshes to  
647 model tropical cyclones in the community atmosphere model. *Mon. Wea. Rev.*, **142** (3), 1221–  
648 1239, doi:10.1175/MWR-D-13-00179.1.
- 649 Zarzycki, C. M., M. N. Levy, C. Jablonowski, J. R. Overfelt, M. A. Taylor, and P. A. Ullrich,  
650 2014b: Aquaplanet experiments using cam's variable-resolution dynamical core. *J. Climate*,  
651 **27** (14), 5481–5503, doi:10.1175/JCLI-D-14-00004.1.
- 652 Zhang, K., and Coauthors, 2017: Impact of numerical choices on water conservation in the e3sm  
653 atmosphere model version 1 (eam v1). *Geoscientific Model Development Discussions*, **2017**,  
654 1–26, doi:10.5194/gmd-2017-293.

## 655 LIST OF FIGURES

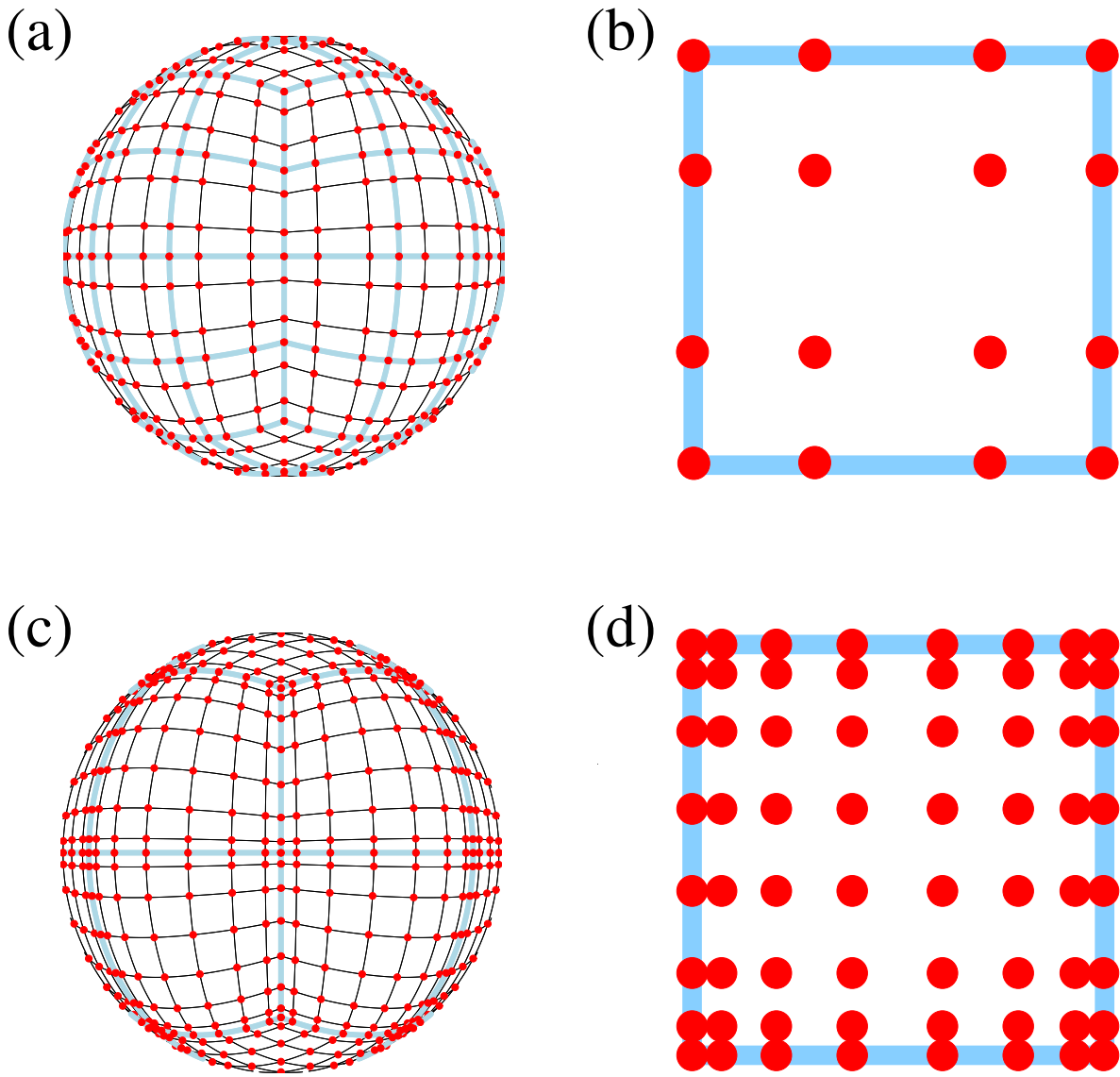
- 656 **Fig. 1.** Example of CAM-SE GLL quadrature grids, marked with red filled circles, (a & c) on the  
 657 cubed-sphere and (b & d) in an element. (a)-(b) and (c)-(d) use  $4 \times 4$  ( $np = 4$ ) and  $8 \times 8$   
 658 ( $np = 8$ ) GLL quadrature points in each element, respectively. (a) and (c) have the same  
 659 average grid-spacing at the Equator ( $7.5^\circ$ ) which is obtained by using (a)  $4 \times 4$  ( $ne = 4$ )  
 660 and (b)  $2 \times 2$  ( $ne = 2$ ) elements on each cubed-sphere face/panel, respectively. The element  
 661 boundaries are marked with thick light blue lines. The grid configurations shown on (a) and  
 662 (c) are referred to as  $ne4np4$  and  $ne2np8$ , respectively. . . . . 25
- 663 **Fig. 2.** A one-dimensional schematic showing the relationship between the basis functions, the  
 664 quadrature nodes and the proposed physics grid, over the coarse of a time-step. The filled  
 665 circles are the GLL quadrature points in each element, which are connected by a Lagrange  
 666 polynomials basis (curves). (a) Smooth initial condition are (b) advanced by the dynamics  
 667 one Runge-Kutta step (blue), and (c) shows the solution after applying the DSS operator.  
 668 Applying (d) grid-scale forcing to an element boundary node, (e) the basis representation is  
 669 clearly  $C^0$  at the element boundary. In contrast, (d) applying grid-scale forcing to an interior  
 670 node (e) results in a smooth,  $C^\infty$  continuous field. (f),(i) Vertical bars pertain to the values  
 671 on the physics grid, found through integrating the basis functions over the control volumes. . . . . 26
- 672 **Fig. 3.** Probability density distribution of instantaneous upward  $\omega$  in a pair of aqua-planet simu-  
 673 lations using CAM4 physics. Figure is constructed from one year of six hourly data, at  
 674 all vertical levels. (a)  $ne30np4$  configuration conditionally sampled for interior, edge and  
 675 corner node control volumes, and similarly (b) for the  $ne30pg3$  configuration. Note the con-  
 676 sistent larger magnitude  $\omega$  for boundary nodes compared with interior nodes in (a), and  
 677 that the bias is substantially reduced through mapping to a quasi-equal area physics grid. . . . . 27
- 678 **Fig. 4.** An example of control volumes constructed around GLL quadrature points ( $ne4np4$ ) so that  
 679 the spherical area of the control volumes exactly match the quadrature weight multiplied by  
 680 the metric factor. . . . . 28
- 681 **Fig. 5.** A schematic illustration of an element, indicating the relationship between (left) the dy-  
 682 namical core grid, and (right) the proposed quasi-equal area physics grid. The physics grid  
 683 contains  $pg \times pg = 3 \times 3$  grid cells in each element. . . . . 29
- 684 **Fig. 6.**  $L_2$  difference norms of the surface pressure field,  $p_s$ , in the moist baroclinic wave simu-  
 685 lations.  $L_2$  values lying within the yellow region fall below the estimate of the uncertainty in  
 686 the reference solution (black curve), computed as the difference norm between two approx-  
 687 imately  $0.25^\circ$  resolution versions of CAM, the spectral-element and finite-volume (CAM-  
 688 FV) dynamical cores. . . . . 30
- 689 **Fig. 7.** Results of the terminator “toy”-chemistry test. Snapshot of the total column integrated,  
 690 weighted sum of the species,  $\langle Cl_y \rangle = \langle Cl \rangle + \langle 2Cl_2 \rangle$ , in kg/kg, at day 15 of the moist baro-  
 691 clinic wave test. (Top) CAM-SE, (Bottom) CAM-SE-CSLAM. . . . . 31
- 692 **Fig. 8.** Climatological zonal-mean total precipitation rate in the aqua-planets, computed from a pair  
 693 of year long simulations. . . . . 32
- 694 **Fig. 9.** Mean (left) and variance (right) of the low level temperature tendencies from the physical  
 695 parameterizations on the GLL grid, with the  $ne30np4$  configuration, (top row) and  $ne30pg3$   
 696 configuration (bottom row), in a pair of year-long aqua-planet simulations after Medeiros  
 697 et al. (2016). Grid imprinting is observed along the element boundaries in  $ne30np4$ , but is  
 698 absent from the  $ne30pg3$  simulation. . . . . 33

- 699 **Fig. 10.** Mean  $\omega$  at two model levels in the middle troposphere, in a Held-Suarez configuration  
 700 outfitted with real world topography. (Left) CAM-SE state on the GLL grid, *ne30np4*,  
 701 (Middle) CAM-SE-CSLAM state on the GLL grid, *ne30np4* and (Right) CAM-SE-CSLAM  
 702 state on the physics grid, *ne30pg3*. The  $\omega$  fields are computed from a 1200 day Held-Suarez  
 703 simulation. The data are contoured according to a ‘cell fill’ approach, in which the coupler  
 704 grids (e.g., Figure ??) are used to delineate the vertices of the control volumes. . . . . 34

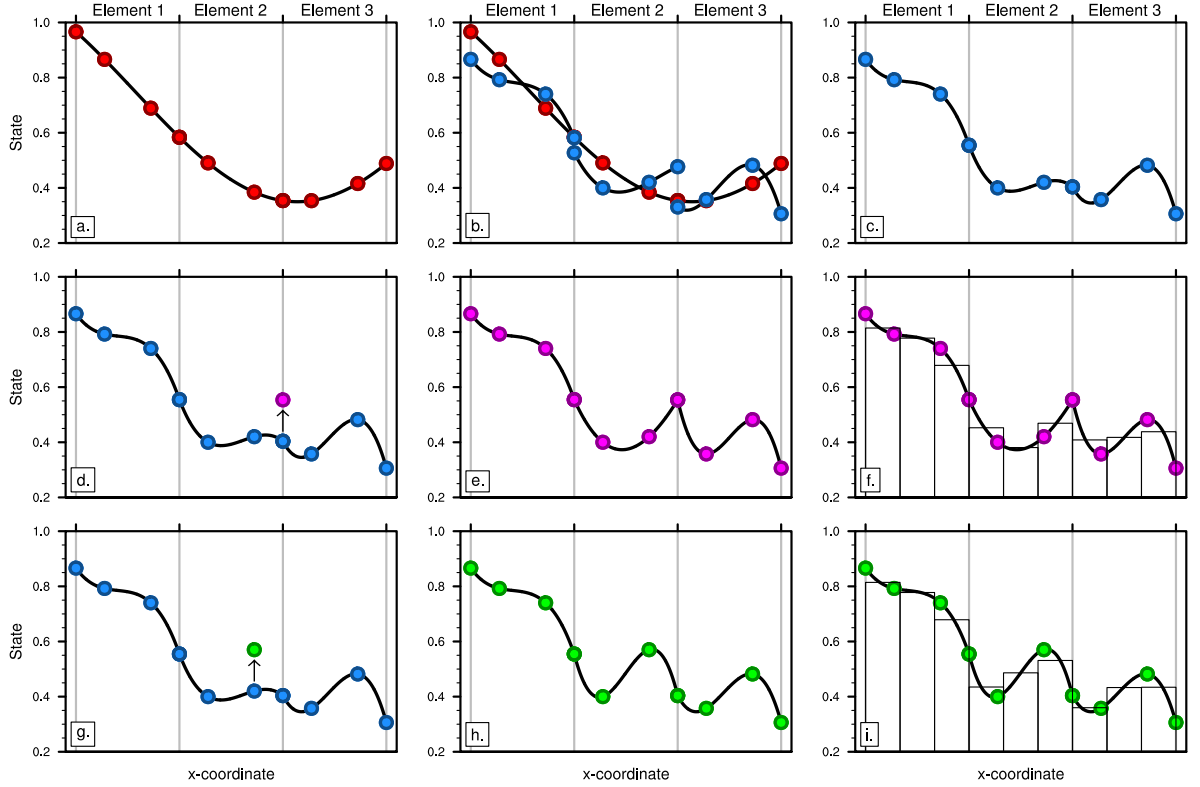
705 **Fig. 11.** Climatological total precipitation rate (in mm/day) computed from the final 19 years of a pair  
 706 of 20 year long AMIP type simulations. (Left) CAM-SE, (middle) CAM-SE-CSLAM and  
 707 (Right) their differences. The difference field is computed through bilinearly interpolating  
 708 to a common latitude-longitude grid. . . . . 35

709 **Fig. 12.** Climatological total precipitation rate computed from the final 19 years of a suite of 20  
 710 year long AMIP simulations, using CAM-SE (*ne30np4*), CAM-SE-CSLAM (*ne30np3*) and  
 711 CAM-FV (*f09*). The top plot is an observational product, the gridded GPCP climatological  
 712 precipitation dataset. . . . . 36

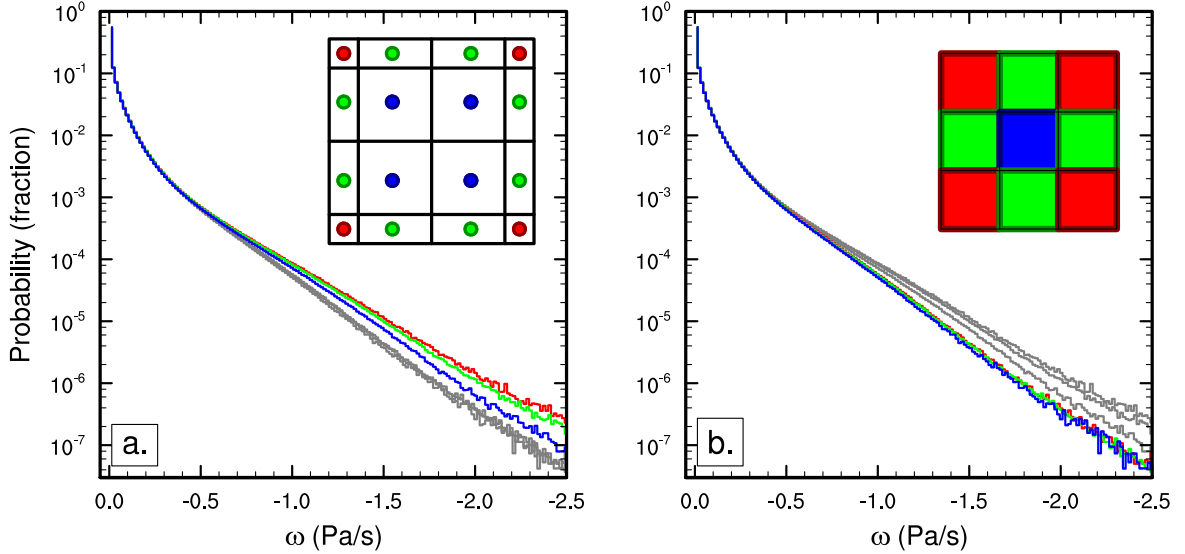
713 **Fig. 13.** Schematic of the coordinate system in which the dimensionally split cubic Lagrange in-  
 714 terpolation is computed. The physics grid centers are marked with asterisks and the GLL  
 715 points, we are interpolating to, with solid filled circles. The element in which the GLL  
 716 points are located is bounded by thick black lines and located in the lower left corner of a  
 717 panel. The stippled lines mark the boundaries of the remaining elements. For simplicity we  
 718 are using the normalized coordinate centered at the element on which the GLL points we  
 719 are interpolating to are located. Note that the coordinates for points on neighboring panels  
 720 (using a different local coordinate system) must be transformed to the coordinate system of  
 721 the element in question. . . . . 37



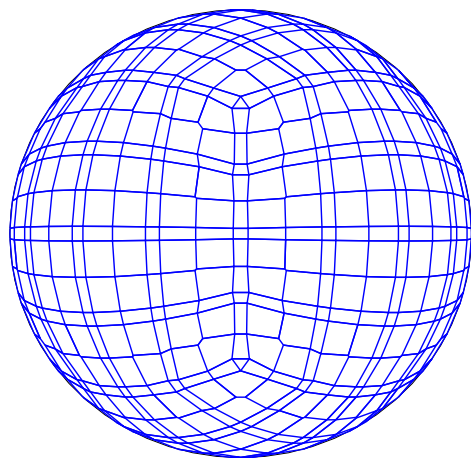
722 FIG. 1. Example of CAM-SE GLL quadrature grids, marked with red filled circles, (a & c) on the cubed-  
 723 sphere and (b & d) in an element. (a)-(b) and (c)-(d) use  $4 \times 4$  ( $np = 4$ ) and  $8 \times 8$  ( $np = 8$ ) GLL quadrature  
 724 points in each element, respectively. (a) and (c) have the same average grid-spacing at the Equator ( $7.5^\circ$ ) which is  
 725 obtained by using (a)  $4 \times 4$  ( $ne = 4$ ) and (b)  $2 \times 2$  ( $ne = 2$ ) elements on each cubed-sphere face/panel, respectively.  
 726 The element boundaries are marked with thick light blue lines. The grid configurations shown on (a) and (c) are  
 727 referred to as  $ne4np4$  and  $ne2np8$ , respectively.



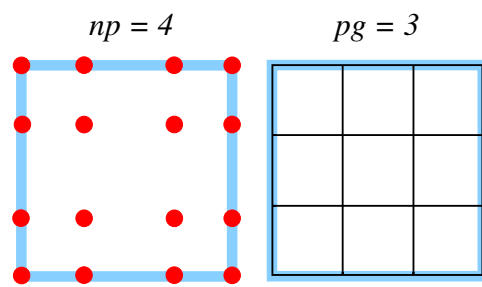
728 FIG. 2. A one-dimensional schematic showing the relationship between the basis functions, the quadrature  
 729 nodes and the proposed physics grid, over the coarse of a time-step. The filled circles are the GLL quadrature  
 730 points in each element, which are connected by a Lagrange polynomials basis (curves). (a) Smooth initial con-  
 731 dition are (b) advanced by the dynamics one Runge-Kutta step (blue), and (c) shows the solution after applying  
 732 the DSS operator. Applying (d) grid-scale forcing to an element boundary node, (e) the basis representation is  
 733 clearly  $C^0$  at the element boundary. In contrast, (d) applying grid-scale forcing to an interior node (e) results  
 734 in a smooth,  $C^\infty$  continuous field. (f),(i) Vertical bars pertain to the values on the physics grid, found through  
 735 integrating the basis functions over the control volumes.



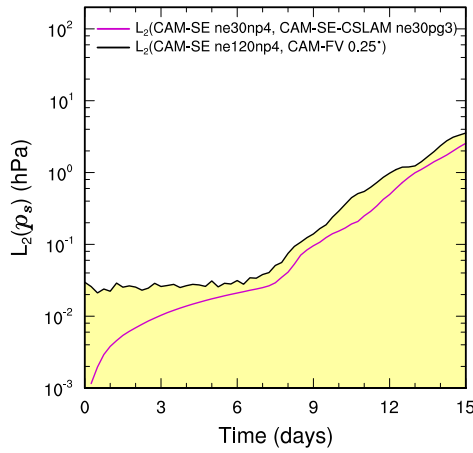
736 FIG. 3. Probability density distribution of instantaneous upward  $\omega$  in a pair of aqua-planet simulations using  
 737 CAM4 physics. Figure is constructed from one year of six hourly data, at all vertical levels. (a) *ne30np4*  
 738 configuration conditionally sampled for interior, edge and corner node control volumes, and similarly (b) for the  
 739 *ne30pg3* configuration. The curves in (a) are overlain in (b) in grey, and similarly the curves in (a) are overlain  
 740 in (b). Note the consistently larger magnitude  $\omega$  for boundary nodes compared with interior nodes in (a), and  
 741 that the bias is substantially reduced through mapping to a quasi-equal area physics grid.



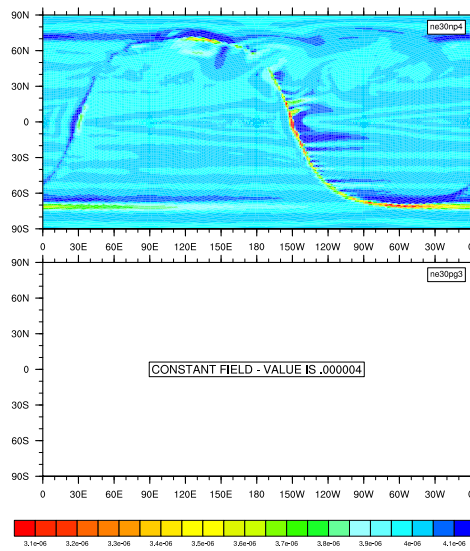
742 FIG. 4. An example of control volumes constructed around GLL quadrature points ( $ne4np4$ ) so that the  
743 spherical area of the control volumes exactly match the quadrature weight multiplied by the metric factor.



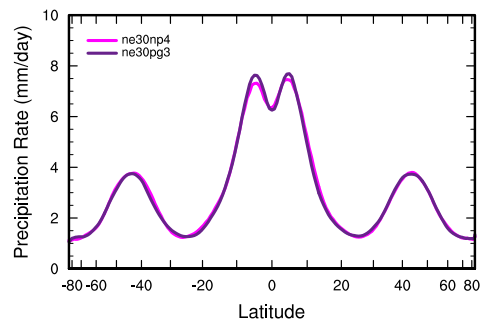
744 FIG. 5. A schematic illustration of an element, indicating the relationship between (left) the dynamical core  
 745 grid, and (right) the proposed quasi-equal area physics grid. The physics grid contains  $pg \times pg = 3 \times 3$  grid cells  
 746 in each element.



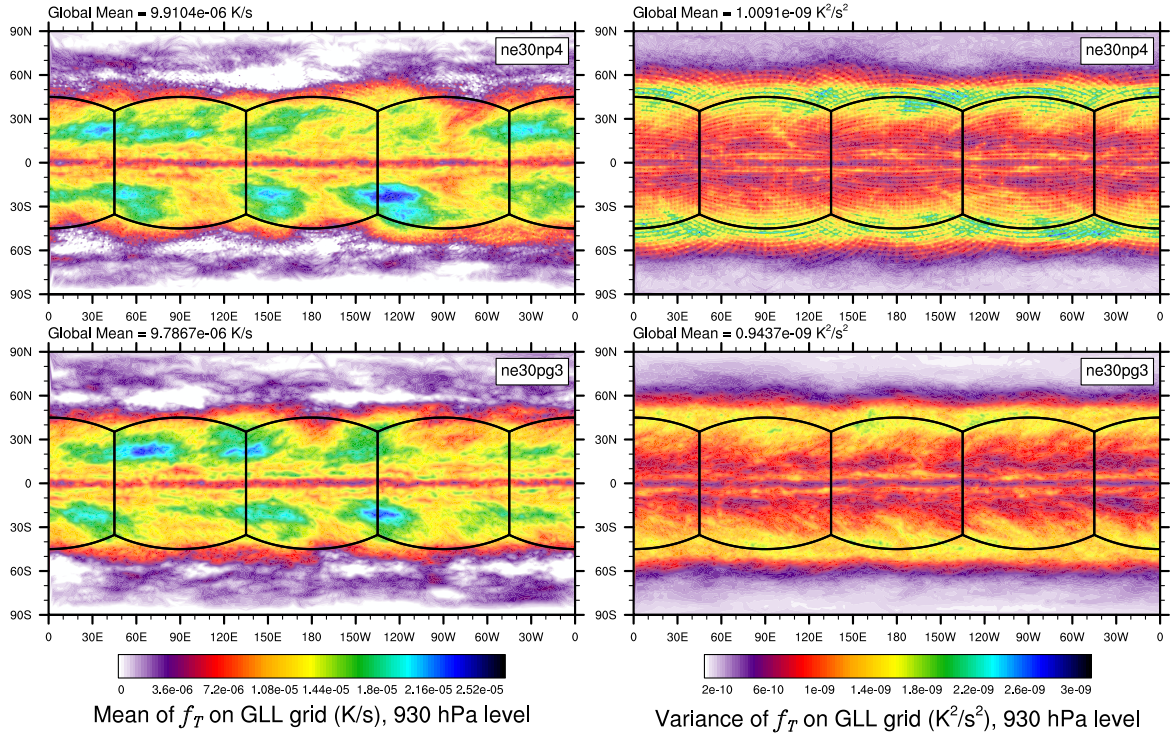
747 FIG. 6.  $L_2$  difference norms of the surface pressure field,  $p_s$ , in the moist baroclinic wave simulations.  $L_2$   
 748 values lying within the yellow region fall below the estimate of the uncertainty in the reference solution (black  
 749 curve), computed as the difference norm between two approximately  $0.25^\circ$  resolution versions of CAM, the  
 750 spectral-element and finite-volume (CAM-FV) dynamical cores.



751 FIG. 7. Results of the terminator “toy”-chemistry test. Snapshot of the total column integrated, weighted sum  
 752 of the species,  $\langle Cl_y \rangle = \langle Cl \rangle + \langle 2Cl_2 \rangle$ , in kg/kg, at day 15 of the moist baroclinic wave test. (Top) CAM-SE,  
 753 (Bottom) CAM-SE-CSLAM.



754 FIG. 8. Climatological zonal-mean total precipitation rate in the aqua-planets, computed from a pair of year  
755 long simulations.



756 FIG. 9. Mean (left) and variance (right) of the low level temperature tendencies from the physical parameteri-  
 757 zations on the GLL grid, with the *ne30np4* configuration, (top row) and *ne30pg3* configuration (bottom row), in  
 758 a pair of year-long aqua-planet simulations after Medeiros et al. (2016). Grid imprinting is observed along the  
 759 element boundaries in *ne30np4*, but is absent from the *ne30pg3* simulation.

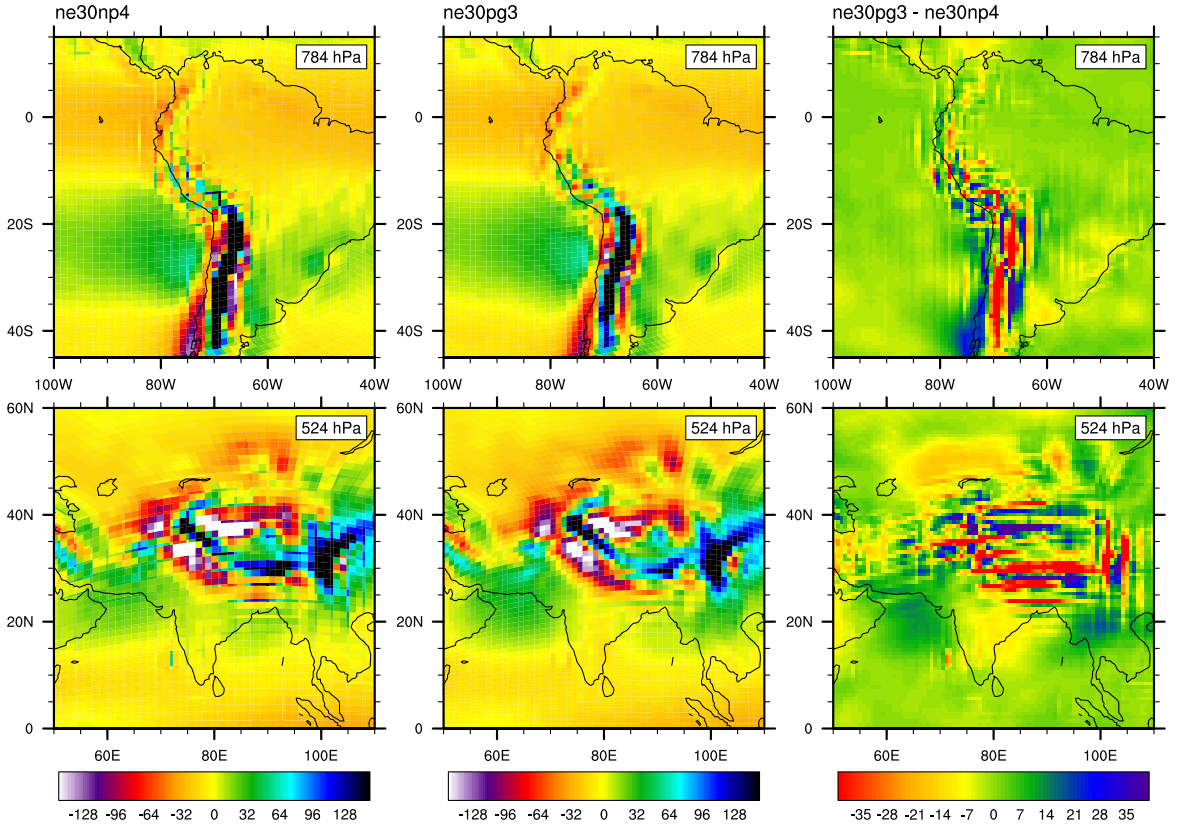
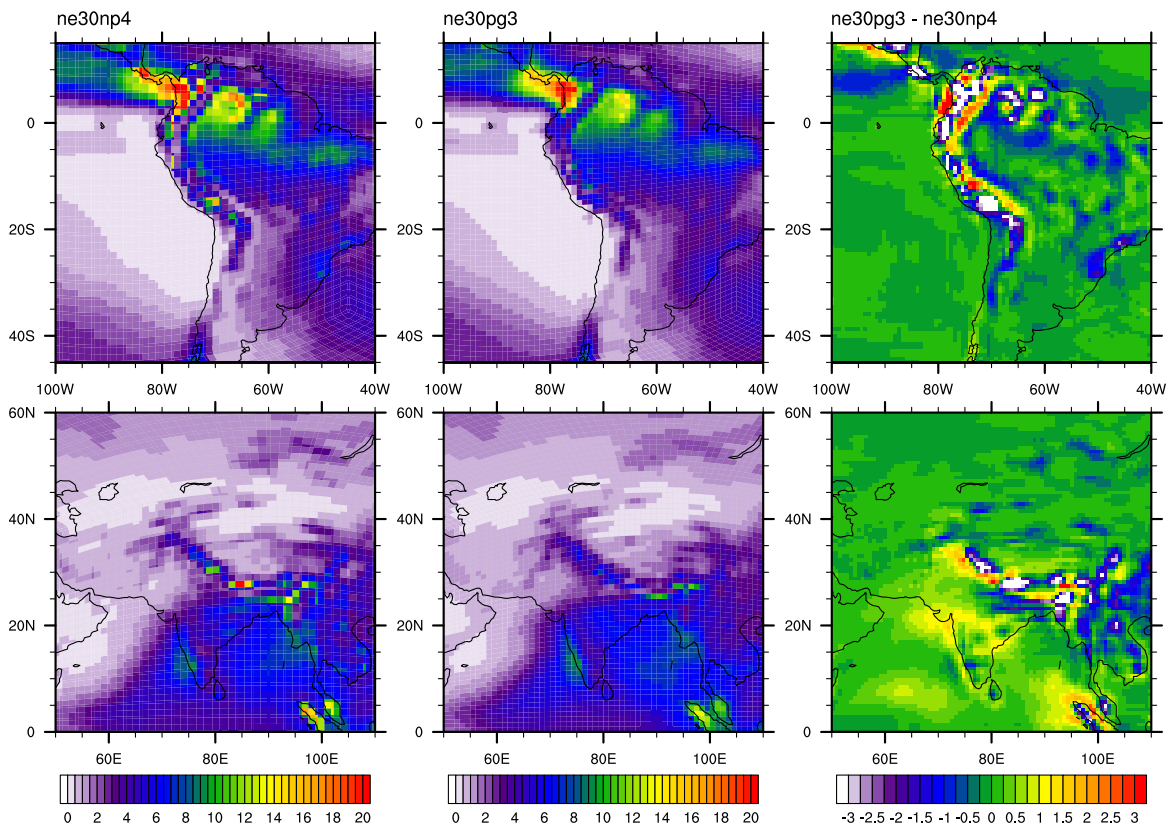
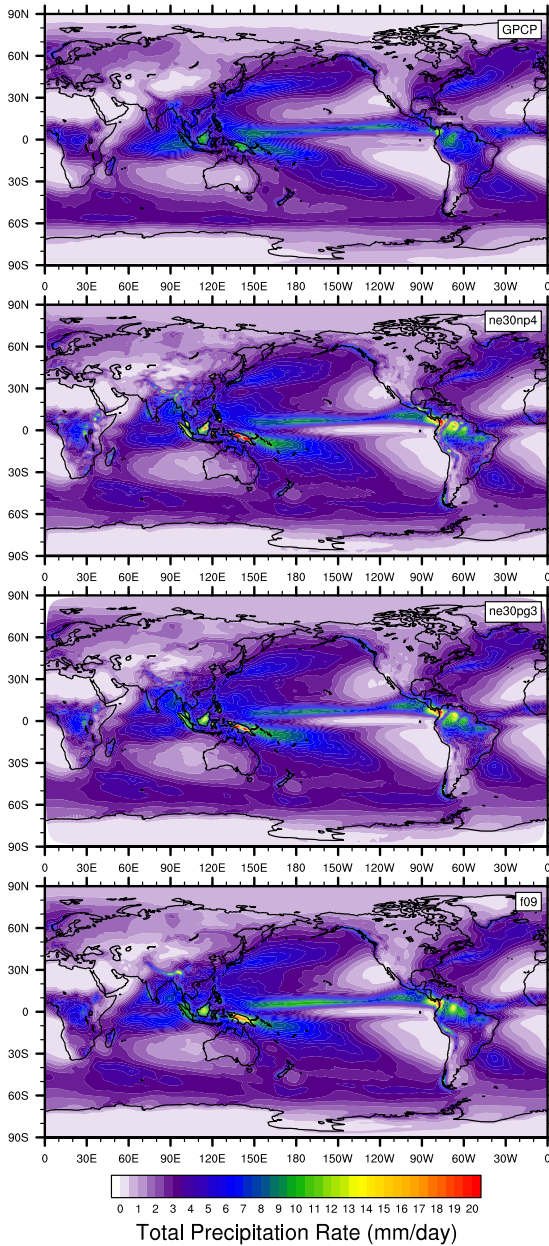


FIG. 10. Mean  $\omega$  at two model levels in the middle troposphere, in a Held-Suarez configuration outfitted with real world topography. (Left) CAM-SE state on the GLL grid, *ne30np4*, (Middle) CAM-SE-CSLAM state on the physics grid, *ne30pg3* and (Right) **their differences computed through bi-linear interpolation to a common latitude-longitude grid**. The  $\omega$  fields are computed from a 1200 day Held-Suarez simulation. The data are contoured according to a ‘cell fill’ approach, in which the coupler grids (e.g, Figure 4) are used to delineate the vertices of the control volumes.



766 FIG. 11. Climatological total precipitation rate (in mm/day) computed from the final 19 years of a pair of 20  
 767 year long AMIP type simulations. (Left) CAM-SE, (middle) CAM-SE-CSLAM and (Right) their differences.



768 FIG. 12. Climatological total precipitation rate computed from the final 19 years of a suite of 20 year long  
 769 AMIP simulations, using CAM-SE (ne30np4), CAM-SE-CSLAM (ne30pg3) and CAM-FV (f09). The top plot  
 770 is an observational product, the gridded GPCP climatological precipitation dataset.

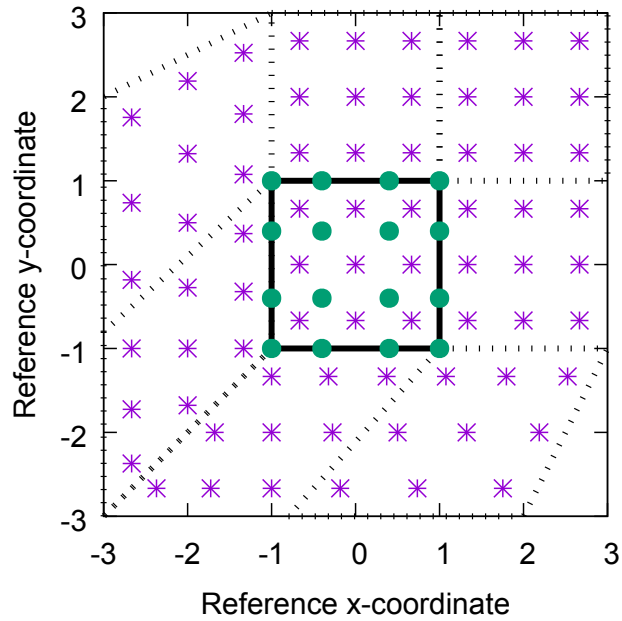


FIG. 13. Schematic of the coordinate system in which the dimensionally split cubic Lagrange interpolation is computed. The physics grid centers are marked with asterisks and the GLL points, we are interpolating to, with solid filled circles. The element in which the GLL points are located is bounded by thick black lines and located in the lower left corner of a panel. The stippled lines mark the boundaries of the remaining elements. For simplicity we are using the normalized coordinate centered at the element on which the GLL points we are interpolating to are located. Note that the coordinates for points on neighboring panels (using a different local coordinate system) must be transformed to the coordinate system of the element in question.